



## Article

**Cite this article:** Fedders ER, Mahoney AR, Dammann DO, Polashenski C, Hutchings JK (2024). Two-dimensional thermal and dynamical strain in landfast sea ice from InSAR: results from a new analytical inverse method and field observations. *Annals of Glaciology* **65**, e28, 1–14. <https://doi.org/10.1017/aog.2024.29>

Received: 31 December 2023

Revised: 19 June 2024

Accepted: 29 July 2024

**Keywords:**



remote sensing; sea-ice geophysics

**Corresponding author:**

Emily R. Fedders;

Email: [erfedders@alaska.edu](mailto:erfedders@alaska.edu)

# Two-dimensional thermal and dynamical strain in landfast sea ice from InSAR: results from a new analytical inverse method and field observations

Emily R. Fedders<sup>1</sup> , Andrew R. Mahoney<sup>1</sup> , Dyre Oliver Dammann<sup>2</sup>, Chris Polashenski<sup>3,4</sup> and Jennifer K. Hutchings<sup>5</sup>

<sup>1</sup>Geophysical Institute, University of Alaska Fairbanks, Fairbanks, AK, USA; <sup>2</sup>Department of Remote Sensing and Geophysics, Norwegian Geotechnical Institute, Oslo, Norway; <sup>3</sup>Alaska Projects Office, Cold Regions Research and Engineering Laboratory, US Army Corps of Engineers, Fort Wainwright, AK, USA; <sup>4</sup>Thayer School of Engineering, Dartmouth College, Hanover, NH, USA and <sup>5</sup>College of Earth Ocean and Atmospheric Sciences, Oregon State University, Corvallis, OR, USA

**Abstract**

Observing continuous strain in sea ice at geophysical scales of tens of meters to kilometers requires displacement measurements made with millimeter-scale precision. Satellite-based interferometric synthetic aperture radar (InSAR) provides such precise measurements of relative surface displacement over broad spatial areas at regular intervals and, unlike point displacement measurements, it allows confident delineation of continuously deforming regions. However, InSAR only captures the 1-D component of surface displacement parallel to a radar's lines-of-sight. Additional analysis is required to translate between these 1-D observations and the horizontal or vertical displacements they arose from. Previous studies utilize an iterative inverse model to constrain estimates of horizontal surface displacement from InSAR. Here we build upon that work outlining a new analytical inverse modeling method for quantifying displacement and strain over continuous regions of sea ice and provide comparison between model results and independent displacement observations. We demonstrate the inverse method over both landfast and drifting ice along the Alaskan coastline. These intercomparisons highlight environments in which displacements inverted from interferograms may be used as an independent estimator of surface strain, as well as the potential for the outlined inverse methods to be used in conjunction with other observing methods.

**1. Introduction**

Sea ice routinely undergoes deformation in response to wind, ocean drag and internal stresses. These deformations may be accommodated by displacement across new or existing fractures, or by elastic strain or viscous creep within mechanically continuous ice. Sea-ice displacement measurements compiled from synthetic aperture radar images (e.g. Kwok, 2001) show that the majority of pack ice deformation at the basin scale is accommodated along oriented fracture systems, termed linear kinematic features (LKFs). Commonly used continuum sea-ice models such as those based on viscous-plastic (e.g. Hibler, 1979) or elasto-brittle (e.g. Dansereau and others, 2016) rheologies describe deformation at cracks and leads in aggregate without directly treating the elastic or viscous strains between these features. These continuum models can reproduce key statistical properties of the basin-scale sea-ice displacement field such as the concentration of strain in oriented LKFs (Hutchings and others, 2005; Dansereau and others, 2016), though the bulk parameterizations of the stress–strain rate relationship used require empirical constraint for parameters that are unmeasurable or non-physical. Also, at progressively smaller scales, details not captured by continuum models, such as the accumulation of strain prior to brittle failure and the timing and location of individual fracture events become important to the decision-making of stakeholders operating on or traveling through the ice pack. Observations of these details of the strain field, such as those we present here, in combination with observations of in-ice stress or environmental forcing would help improve our understanding of sea-ice rheology at local and regional scales, aiding development and calibration of finite (e.g. McKenna and others, 2021) and discrete element models (Damsgaard and others, 2018; West and others, 2022).

Continuous strains typically involve much smaller displacements than deformation accommodated across fractures. Sea ice, with an elastic modulus on the order of  $10^9$  Pa and compressive strength on the order of  $10^4$  Pa (Timco and Weeks, 2010), may support continuous elastic strain magnitudes up to the order of  $10^{-5}$ , although viscous strains may accumulate over time to larger magnitudes. Observing both varieties of continuous strains at geophysical length scales of kilometers in the field therefore requires the ability to measure changes in distance with a precision of centimeters or better. This required sensitivity poses technological and logistical challenges. Point measurements of displacement collected with laser-based, field-capable surveying technology, such as that used by Parno and others (2022) provide

© The Author(s), 2024. Published by Cambridge University Press on behalf of International Glaciological Society. This is an Open Access article, distributed under the terms of the Creative Commons Attribution licence (<http://creativecommons.org/licenses/by/4.0/>), which permits unrestricted re-use, distribution and reproduction, provided the original article is properly cited.

[cambridge.org/aog](https://www.cambridge.org/aog)



millimeter-scale precision, allowing measurement of continuous strains over distances of hundreds of meters to kilometers. However, the effective range of such survey systems is limited to  $\sim 1\text{--}2$  km and the number of observations within this range is limited by deployment effort required to tens of points. This results in sparse coverage that makes it difficult to precisely locate individual fractures and determine whether observed deformation is accommodated over continuous or discontinuous ice. These systems thus provide a strain measurement that may be an aggregate of both deformation of continuous ice and displacement across leads and cracks. The work presented here is motivated by the advantages of satellite-based remote-sensing techniques capable of observing continuous strain over wide areas of sea ice while also identifying the locations of fractures. Specifically, we focus here on the use of interferometric synthetic aperture radar (InSAR).

InSAR analysis can detect millimeter-scale changes in line-of-sight distance from the sensor to the Earth's surface between repeat SAR images (Moreira and others, 2013). These images cover large areas of the earth's surface (tens of  $\text{km}^2$ ) at regular repeat intervals, independent of cloud cover and without requiring in situ observations. The spatial coverage provided by a coherent interferometric image allows for identification of mechanically continuous regions of ice bounded by active fractures (e.g. Li and others, 1996). However, because InSAR measures change in line-of-sight distance only, it provides a 1-D measurement of surface displacement occurring in 3-D space. Careful calculations and assumptions about the nature of the observed deformation are required to estimate the displacement field likely to have caused an observed 1-D signal. Additionally, InSAR only yields a coherent and interpretable deformation signal over surfaces that do not experience too much motion relative to the resolution cell size. Coherence is lost when displacement approaches approximately half the width of a resolution cell. Drifting sea ice commonly moves at speeds up to  $1.5\text{ m s}^{-1}$  (Mahoney and others, 2015) and InSAR data are typically processed at resolutions  $\sim 50$  m, so interferometric coherence may last only minutes. Most polar-orbiting interferometric satellites provide a repeat interval of more than a week, largely limiting sea-ice applications of InSAR to non-drifting landfast ice (Meyer and others, 2011; Dammann and others, 2019).

Li and others (1996) utilized ERS-1 interferograms to detect strain discontinuities in landfast ice near Prudhoe Bay, Alaska, and estimate the surface motion between discontinuities as either tilt or shear strain. Scheiber and others (2011) outlined an analytical inversion for estimating the rotation of drifting ice floes. Others have quantified displacement or strain within limited case studies in which the type or orientation of strain is inferred from some observed forcing, such as prevailing wind (Dammert and others, 1998; Morris and others, 1999) or impacts from drifting ice (Dammert and others, 1998; Berg and others, 2015). Dammann and others (2016) outlined an iterative, numerical inverse model for interpreting 2-D horizontal sea-ice strain arising from single deformation modes from interferograms over landfast ice. Model validation by comparison with GNSS point displacement measurements was provided by Dammann and others (2018). It is timely to expand on this work considering continued and planned InSAR-capable satellite missions and the unique ability of InSAR to evaluate local-scale continuous sea-ice dynamics. Toward this end, we present an analytical inverse modeling method for quantifying the mode, magnitude and orientation of horizontal strain in sea ice arising from both single and combined deformation modes.

We use this analytical inverse approach to derive horizontal sea-ice displacement and strain from 12 d Sentinel-1 interferograms over Elson Lagoon, Alaska, USA east of Point Barrow, and 10 s

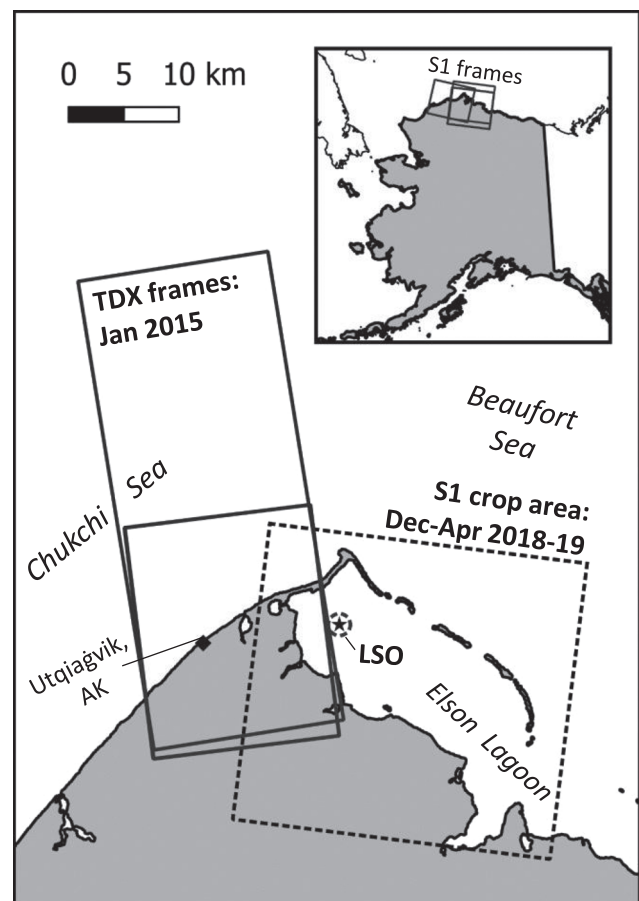


**Figure 1.** Map illustrating the locations of our two study sites in Elson Lagoon and the Chukchi Sea. Solid boxes show extents of TanDEM-X (TDX) and Sentinel 1 interferograms used. The dashed box indicates the area utilized from Sentinel 1 interferograms, and the dashed circle illustrates the extent of the LSO retroreflector array.

TDX interferograms acquired over the Chukchi Sea west of Utqiagvik, Alaska (Fig. 1). For validation, we compare inverse model results over Elson Lagoon to independent, contemporaneous point displacement observations. We lack a similar validation dataset for our Chukchi site but instead explore several displacement solutions and use a process of elimination to arrive at a likely result.

## 2. Study sites

### 2.1 Elson Lagoon

Elson Lagoon is bounded by the Alaska mainland to the southwest and a chain of barrier islands to the northeast. Sea ice in the lagoon is landlocked (Hata and Tremblay, 2015a, 2015b; Mahoney, 2018) between these boundaries throughout much of the frozen season. The barrier islands protect the landlocked ice from dynamic interactions with passing pack ice and prevent the lagoon ice from breaking away from shore. This protection makes the lagoon a relatively stable platform on which to deploy monitoring equipment for season-long observational campaigns. The Sea Ice Dynamics Experiment (SIDEx) team executed such a campaign during the winter of 2018/19 with the aim of measuring thermal stress, strain and fracture in the lagoon ice over the course of a winter season. Measurements of strain from this SIDEx campaign discussed in Section 3.3 are key to this study, providing an independent observation against which to compare modeled displacements.

## 2.2 Chukchi Sea near Utqiagvik, Alaska

Our Chukchi Sea study area contains both drifting and landfast ice along a stretch of open coastline offshore from Utqiagvik, Alaska. Without the protection of barrier islands, landfast ice in this area frequently undergoes dynamic interactions with drifting pack ice. These interactions deform the landfast ice and alter the location of the landfast ice edge several times a season (e.g. Mahoney and others, 2007).

## 3. Datasets

### 3.1 12 d Sentinel-1 interferograms over Elson Lagoon

The Sentinel 1 (S1) A and B satellite constellation, operated by the European Space Agency, transmits in the C-band with a wavelength of 5.55 cm. Each satellite provides a 12 d repeat pass for creating A–A or B–B interferograms. We used the Alaska Satellite Facility's Hybrid Pluggable Processing Pipeline (HyP3) (Hogenson and others, 2016) to create fifteen 12 d interferograms over Elson Lagoon from Sentinel 1 image pairs acquired in interferometric wide swath mode between 24 December 2018 and 27 April 2019. Attributes of these images are listed in Supplementary Table S1. HyP3 is a web-based, on-demand platform which performs all interferogram production steps ([https://hyp3-docs.asf.alaska.edu/guides/insar\\_product\\_guide/](https://hyp3-docs.asf.alaska.edu/guides/insar_product_guide/)), including multi-look by 10 pixels across-track and 2 pixels along-track to give a final image resolution of 80 m and pixel spacing of 40 m. HyP3 also performs adaptive filtering to improve interferogram coherence, and geocodes each interferogram to automatically assigned UTM zones 4 or 5 with 40 m square pixels. We further smooth each interferogram by taking the moving average of a 5 × 5 pixel window in complex space.

### 3.2 10 s TanDEM-X interferograms over the Chukchi Sea

Along the Chukchi coast we utilize shorter, 10 s interferograms from the German Aerospace Center's (DLR) Tan-DEM-X (TDX) satellite constellation operated in Stripmap Pursuit Monostatic mode. While the satellites only operated in this mode for a few months in 2010 (Scheiber and others, 2011), and from October 2014 to March 2015, these 10 s interferograms provide a unique opportunity to use InSAR to quantify surface strain over drifting sea ice.

The TDX satellites operate in the X-band with a wavelength of 3.11 cm. Attributes of the three image pairs used here, acquired between 6 January 2015 and 22 January 2015 are listed in the Supplementary material (Table S2). We follow a similar InSAR processing workflow to that carried out by the HyP3 interface. We co-register each TDX image pair and multi-look each image by 4 pixels across-track and 2 pixels along-track to give an approximate resolution of 10 m. We apply an adaptive filter (Goldstein and Werner, 1998) to each interferogram to improve coherence, and georeference each to a zone 4 UTM grid with 5 m square pixels.

### 3.3 Laser strain observatory measurements of surface displacement in Elson Lagoon

A laser strain observatory (LSO) consisting of a Leica TM-50 total station and array of retro-reflecting prisms provide point displacement measurements on Elson Lagoon throughout the winter 2018/19 SIDEx field campaign. The prisms were mounted on steel posts anchored in the ice at distances of 40–929 m from the central total station and spaced through 360° of azimuth. The total station recorded range, azimuth and zenith to each of 23 retroreflectors at several-minute intervals (dependent on the

time taken to locate each reflector in series) from 19 December 2018 to 20 May 2019, with a gap from 23 December 2018 to 16 January 2019 due to a technical issue. The location of the central total station was recorded at the time of deployment using a wide area augmentation system (WAAS) enabled handheld GPS with expected precision of ±3 m. We use this position to locate the LSO array in the UTM projection of each Sentinel 1 interferogram over Elson Lagoon.

The central total station has a manufacturer-stated theoretical accuracy of  $1.6 \times 10^{-6}$  m ( $0.6 \text{ mm} + 1 \text{ mm km}^{-1}$ ) in range, and  $1.4 \times 10^{-4}$  degrees in azimuth ( $2.4 \text{ mm}$  at 1 km). Consecutive range measurements during periods of little deformation or atmospheric change show range measurement repeatability approaches  $10^{-7}$  m. We correct for range errors caused by variations in air temperature, pressure or humidity using a correction factor calculated from measurements of these parameters collected at an on-site weather station. Calculated correction factors are expected to be accurate to  $\pm 1 \text{ mm km}^{-1}$ . We therefore expect practical field accuracy in absolute range near  $2 \times 10^{-6}$  m. We also correct azimuth positions of retroreflectors for gradual drift by subtracting any rotations experienced uniformly by a majority of the reflectors from the azimuth positions of all reflectors.

## 4. Principals of InSAR for sea-ice monitoring

### 4.1 Contributions to interferometric phase

A radar signal traveling from a sensor to a scattering surface and back returns to the sensor at some position, called phase, in the radar waveform, recorded as an angle between  $-\pi$  and  $\pi$  radians. InSAR analysis evaluates pixel-by-pixel differences in returned phase between two coherent and aligned SAR images to create an interferogram (Moreira and others, 2013). These phase differences, called interferometric phase,  $\phi$ , are caused by real or apparent changes in line-of-sight signal path length from the sensor to the surface,  $\Delta r$ , between images:

$$\phi = \frac{4\pi(\Delta r \cos(\lambda/2))}{\lambda} \quad (1)$$

Like the returned phase in each interfered image,  $\phi$  is a circular value, wrapping over an interval of  $2\pi$  radians. If  $\Delta r$  is smoothly varying and differences between neighboring pixels are small ( $\ll \lambda/2$ ),  $\phi$  creates patterns of phase wraps called fringes across an interferogram. Over such areas, phase can be unwrapped to remove the  $2\pi$  ambiguity in Eqn (1), allowing evaluation of relative differences in  $\Delta r$  between pixels.

Observed  $\phi$  across an interferogram is the sum of several components arising from different processes that alter the real or apparent range,  $r$ , from the sensor to the surface:

$$\phi = \phi_{\text{def}} + \phi_{\text{topo}} + \phi_{\text{atm}} + \phi_{\gamma} \quad (2)$$

where  $\phi_{\text{def}}$  is the contribution from surface deformation, or strain;  $\phi_{\text{topo}}$  is the contribution from topographic relief;  $\phi_{\text{atm}}$  is the contribution from changing atmospheric conditions and  $\phi_{\gamma}$  is the contribution from decorrelation.

### 4.2 Excluding non-deformation components of phase

In this work, we assume  $\phi_{\text{def}}$  is the primary component of total observed  $\phi$ .

$\phi_{\text{topo}}$  arises from changes in satellite position and varies proportionally to topographic height,  $h_{\text{topo}}$ , and the perpendicular baseline distance,  $B_{\perp}$ , between sensor locations during each

acquisition:

$$\phi_{\text{topo}} = h_{\text{topo}} \frac{4\pi B_{\perp}}{\lambda r \cos(\theta)} \quad (3)$$

In a sea-ice environment, pressure ridges represent the largest topographic variation. The 95th percentile of pressure ridge sail heights across the Arctic is 2 m and modal width is 35 m (Duncan and Farrell, 2022). For typical  $B_{\perp}$  on the order of  $10^2$  m and slant range,  $r$ , on the order of 900 km, such ridges will cause a similar phase response to millimeter-scale line-of-sight displacements. Moreover, since ridges are only one or a few pixels wide, their phase signature cannot be extensively monotonic. We can therefore assume  $\phi_{\text{topo}}$  is negligible where phase gradients are sustained and monotonic over distances greater than tens of meters.

Changes in atmospheric conditions between two acquisitions cause apparent range changes by altering the signal's speed or path curvature, giving rise to an atmospheric component,  $\phi_{\text{atm}}$ . We expect contributions from  $\phi_{\text{atm}}$  to be small in comparison to other components following Dammann and others (2016). Both study sites are in areas with minimal topographic relief (Jolivet and others, 2011, 2014) and  $\phi_{\text{atm}}$  tends to be largest in areas of mountainous terrain. Additionally, the 10 s interval of TDX interferograms provides little time for significant atmospheric change. We therefore do not consider  $\phi_{\text{atm}}$  further.

Finally, thermal instrument noise, temporal and spatial decorrelation, and changes in surface scattering properties between acquisitions contribute to apparent changes in range, leading to a decorrelation component,  $\phi_{\gamma}$ . The expected variance of the decorrelation component  $\phi_{\gamma}$  increases with decreasing coherence,  $\gamma$  (Rosen and others, 2000).  $\gamma$  is a metric of interferometric phase quality, which takes on values between 0, indicating no correlation between primary and secondary interfered images, and 1, indicating that the primary and secondary images contain exactly the same phase (Woodhouse, 2006). We limit the magnitude of  $\phi_{\gamma}$  by limiting our analysis to regions of continuous phase in which more than 75% of pixels maintain complex coherence,  $\gamma, >0.35$ .

#### 4.3 Identification and exclusion of vertically dominated displacement

The line-of-sight component of surface motion may be composed of horizontal displacement,  $d_h$ , and vertical displacement,  $d_v$ , whose contributions to  $\phi_{\text{def}}$  depend on the elevation angle,  $\theta$ , between each pixel and the satellite:

$$\phi_{\text{def}} = \frac{4\pi}{\lambda} (d_h \cos \theta + d_v \sin \theta) \quad (4)$$

Our aim here is to interpret horizontal displacements alone. However, typical SAR elevation angles provide similar sensitivity to both  $d_h$  and  $d_v$ , and gradients in  $d_h$  and  $d_v$  can have similar magnitudes. This means vertical and horizontal displacements can make similar contributions to  $\phi_{\text{def}}$  that are difficult to separate. We therefore need to exclude interferograms containing significant vertical displacements. We do this by limiting our analysis to interferograms or regions of interferograms in which the gradient in  $\phi$  is monotonic along the look direction of the satellite, following Dammann and others (2016). This criterion for assuming  $d_v$  is negligible follows from the observation that gradients in  $d_v$ , or surface tilts, cannot continue indefinitely. Whether arising from sea surface tilt, thermodynamic or dynamic buckling, or wave activity, gradients in  $d_v$  exhibit undulations at length scales of hundreds of m to tens of kilometers (Evans and others, 1971; Kwok and Morison, 2016; Mahoney and others, 2016). Strains are not similarly spatially limited. Therefore, if a phase

gradient is monotonic over tens of kilometers, vertical displacements must be negligible. If the phase gradient exhibits small undulations that do not overwhelm a stronger monotonic gradient, undulations may be filtered out and vertical deformation assumed negligible in the remaining signal. We apply such filtering to TDX interferograms. If the phase gradient exhibits strong undulations relative to the overall phase gradient, such filtering cannot be applied and horizontal and vertical contributions are inseparable without additional information. This is the case in some regions of Elson Lagoon, which we remove from analysis. Wang and others (2020) as well as Chen and others (2021) do present alternative quantitative methods for separating vertical and horizontal sea-ice displacement components using multi-orbit InSAR techniques. However, their methods require the assumption that deformation occurs at a constant rate over the multi-day interval spanned by overlapping InSAR pairs from ascending and descending orbits. The episodic nature of processes causing sea surface tilt and sea-ice deformation means this condition is rarely met and so we do not adopt this approach here.

## 5. Phase unwrapping over regions of smoothly varying phase (RSVPs)

### 5.1 RSVP identification

Unwrapping, or spatially integrating, phase values across continuous RSVPs simplifies inverse model calculations by removing relative  $2\pi$  phase ambiguity. Within an RSVP, or area of sequential, continuous fringes bounded by discontinuities, differences in unwrapped phase between pixels are directly proportional to the line-of-sight component of relative displacement between them. Relative displacement between pixels located in separate RSVPs cannot be evaluated, since an unknown number of phase wraps are lost at RSVP boundaries. We identify RSVPs in each interferogram to allow accurate unwrapping and to delineate where we can or cannot evaluate relative displacements in later steps. Dulam and others (2023) describe recent advancement toward automated RSVP boundary detection in ground-based radar interferograms over sea ice, but similar methods are not operational for satellite-acquired interferograms. Instead, we use the hybrid automated and manual approach described below.

Discontinuities at RSVP boundaries generally appear as an abrupt change in the magnitude or orientation of the phase gradient. To detect these abrupt changes, we first calculate phase gradient components  $\partial\phi/\partial x$  and  $\partial\phi/\partial y$  in complex space using Eqns (5) and (6), following Libert and others (2022). These equations yield an average phase slope over a  $w \times w$  window of pixels, where  $w$  must be odd and  $>1$ . We set  $w = 3$  for maximum gradient resolution and assign the calculated average slope to the center pixel in each window. Calculating the gradient in complex space ensures correct slope magnitude where phase wraps between  $-\pi$  and  $\pi$  radians:

$$\left. \frac{\partial\phi}{\partial x} \right|_{(x_k, y_l)} = \text{atan2} \left( \sum_{m=k-(w-1)/2}^{k+(w-1)/2} \sum_{n=l-(w-1)/2}^{l+(w-1)/2} e^{i(\phi_{m,n+1} - \phi_{m,n})} \right) \quad (5)$$

$$\left. \frac{\partial\phi}{\partial y} \right|_{(x_k, y_l)} = \text{atan2} \left( \sum_{m=k-(w-1)/2}^{k+(w-1)/2} \sum_{n=l-(w-1)/2}^{l+(w-1)/2} e^{i(\phi_{m,n+1} - \phi_{m,n})} \right) \quad (6)$$

We convert  $\partial\phi/\partial x$  and  $\partial\phi/\partial y$  into slope magnitude,  $s$ , and fringe azimuth,  $\alpha_f$ , pairs using Eqns (7) and (8), respectively.  $\alpha_f$  records the direction of the most positive phase slope, perpendicular to lines of fringes in an interferogram, as an angle

counter-clockwise from east:

$$s = \sqrt{\frac{\partial\phi^2}{\partial y} + \frac{\partial\phi^2}{\partial x}} \quad (7)$$

$$\alpha_f = \text{atan2}\left(\frac{\partial\phi}{\partial y}, \frac{\partial\phi}{\partial x}\right) \quad (8)$$

We identify discontinuities where the std dev. of the phase slope over a  $5 \times 5$  pixel moving window exceeds a threshold of  $3.16 \times 10^{-3} \text{ rad m}^{-1}$ . This threshold was chosen as the mean 95th percentile of slope std devs. over coherent ( $\gamma > 0.35$ ) pixels in Elson Lagoon. This threshold is likely not universally generalizable, but worked here to identify most discontinuities without identifying false boundaries due to isolated areas of low coherence. We manually connect detected discontinuities arranged in linear patterns and add any additional obvious discontinuities which were not detected by thresholding. This manual step is important for identifying boundaries between regions where fringe patterns to either side show slopes of similar magnitude, and perhaps even orientation, but are clearly offset from one another. Land pixels in both study areas and pixels beyond the barrier islands in the Elson Lagoon study area are removed using a hand-drawn mask.

### 5.2 Phase unwrapping within RSVPs in Sentinel 1 interferograms

For Sentinel 1 interferograms, once RSVPs are delineated as described above, we unwrap each RSVP individually using a three-step process. We first integrate phase at pixels with coherence  $> 0.2$  using the branch cut unwrapping algorithm provided in the GAMMA software package (Werner and others, 2002). We use adaptive-window interpolation to fill gaps in unwrapped phase where low coherence pixels were skipped. Then we use the unwrapped, filled interferograms as a model for unwrapping the low-coherence pixels using the same branch-cut algorithm as in step 1. We adjust unwrapped phase in each RSVP to have a mean value of zero to obtain appropriate relative displacement magnitudes between points in later steps.

### 5.3 Phase unwrapping within RSVPs in TDX interferograms

For TDX interferograms, we begin by following the same unwrapping method as for Sentinel 1 interferograms. Then we fit a planar surface to each unwrapped RSVP and use this smoothed, planar unwrapped phase for all further analysis. This smoothing step preserves the majority of the phase gradient, which we attribute to horizontal motion, while removing the periodic signals Mahoney and others (2016) show to arise from vertical displacement due to infragravity waves (Fig. 2). A few isolated, non-periodic residual signals found at asperities along RSVP boundaries (e.g. white arrows in Fig. 2), likely indicating elevated strain at these point contact locations, are also lost in the smoothing process. However, these residual signals are spatially confined and contain less than one full phase wrap each, and overall correlation coefficients between original unwrapped phase and fitted, smooth unwrapped phase are  $\geq 0.8$  in 88% of RSVPs.

## 6. Modeling 2-D horizontal sea-ice displacement and strain from single orbit InSAR

### 6.1 Model concept: geometric relationships between displacement and $\phi$

Any sea-ice deformation or displacement in the horizontal plane may be fully described by some combination of five modes: uniaxial convergence, simple shear, isotropic radial convergence, rigid rotation and rigid translation. Divergence is represented as a negative convergence. The fringe pattern in a monotonic interferogram therefore records the sum of one or more component phase gradients associated with each of these horizontal deformation modes:

$$\phi_{\text{def}} = \phi_{\text{ax}} + \phi_{\text{shear}} + \phi_{\text{rad}} + \phi_{\text{rot}} + \phi_{\text{trans}} \quad (9)$$

Each horizontal mode on its own creates phase gradients whose slope,  $s$ , and orientation,  $\alpha_f$ , exhibit defined geometric relationships with satellite look direction,  $\alpha_l$ , deformation magnitude and deformation orientation. Radially symmetric deformation modes produce phase gradients with orientations that depend only on the look direction. Radial convergence leads to phase gradients with  $\alpha_f$  parallel to the look direction such that  $\alpha_f = \alpha_l$  or  $\alpha_f = \alpha_l + \pi$  (Figs 3a, b), while rotation creates phase gradients perpendicular to the look direction such that  $\alpha_f = \alpha_l \pm \pi/2$  (Figs

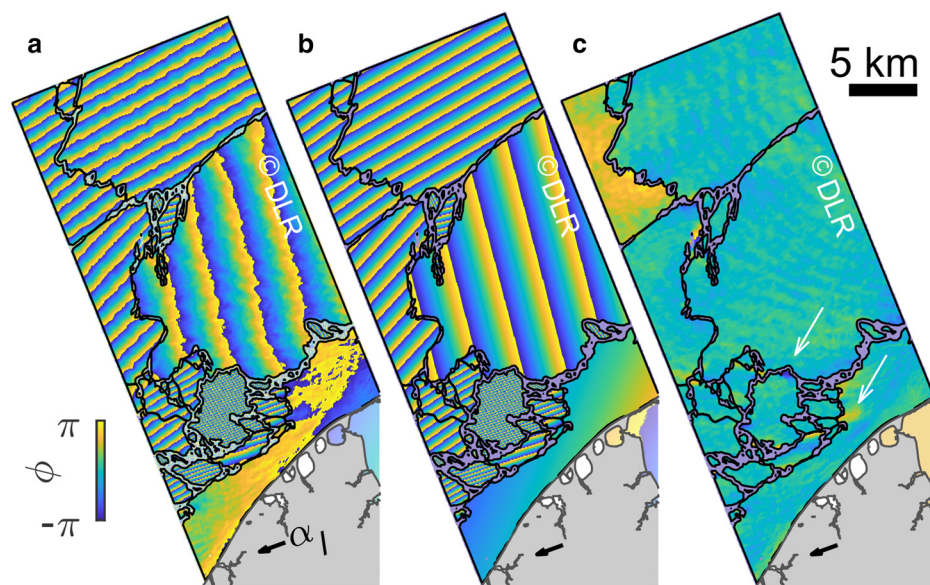


**Figure 2.** TDX interferogram from 6 January 2015 (a) original, wrapped, (b) unwrapped with waves removed, re-wrapped for ease of visual comparison. (c) The residual signal left behind by the unwrapping and smoothing process (panel a minus panel b) contains low amplitude wave signals.

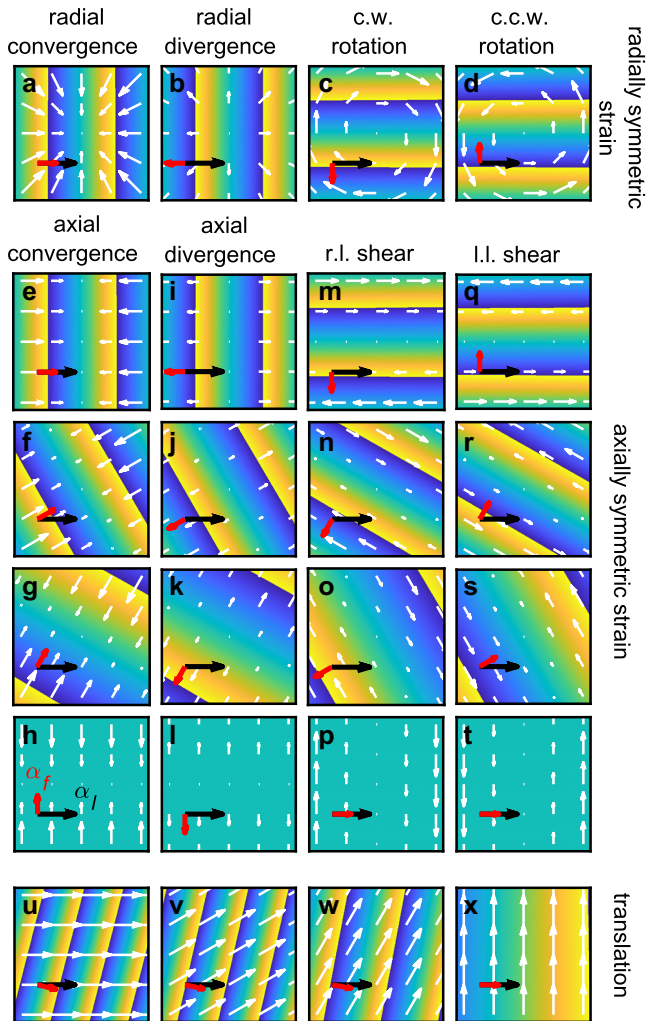


**Figure 3.** Interferometric fringe patterns associated with positive (a) and negative (b) radial convergence, clockwise (c) and counter-clockwise (d) rotations, and with varying orientations of positive (e–h) and negative (i–l) axial convergence, right-lateral (m–p) and left-lateral (q–t) simple shear, and rigid translation (u–x). White arrows show the direction of surface displacements. Black and red arrows mark the look direction,  $\alpha_l$ , and phase gradient azimuth,  $\alpha_f$ . For each mode, all displacement fields represent the same strain magnitude.

3c, d). For these modes, the magnitude of the phase gradient depends directly on the magnitude of the deformation. In contrast, axially symmetric deformation modes (uniaxial convergence and simple shear) produce interferometric phase gradients whose orientation varies with deformation direction and is less strictly tied to  $\alpha_l$  (Figs 3e–t). The magnitude of the phase gradient for these axial modes depends on both the magnitude of deformation and the degree of alignment between  $\alpha_l$  and the direction of surface displacement.

Translation can only produce phase gradients with  $\alpha_f$  parallel to the orientation of the gradient in elevation angle across the image,  $\alpha_\theta$ , which is nearly parallel to  $\alpha_l$ . The magnitude of the phase gradient produced by translation depends strongly not only on the magnitude of the component of displacement parallel to  $\alpha_\theta$ , but also on the magnitude of the elevation angle gradient across an image (Figs 3u–x). This across-track gradient in  $\theta$  also makes a small contribution to phase gradients arising from the radial and axial modes discussed above. However, in those cases where there is a gradient in look parallel displacement, the effect of the gradient in  $\theta$  across the swath is a second-order effect. We use these geometric relationships between deformation characteristics and interferogram characteristics to derive a separate set of analytical inverse equations for each horizontal deformation mode.

However, we also note the ambiguity inherent in inverting 2-D displacements from the 1-D information contained in the interferometric phase gradient. A near-infinite set of 2-D, horizontal displacement fields exists that would reproduce the interferometric pattern in any RSVP exactly. A few examples of this ambiguity are illustrated in Figure 4. For any RSVP, axial convergence and simple shear displacement solutions exist that would reproduce the observed phase gradient exactly, regardless of the mode or modes that contributed to real surface displacement. Similarly, radial convergence, translation and rotation solutions exist that would reproduce the entire look-parallel or look-perpendicular component of the phase gradient, regardless of whether any of these modes contributed at all to the real displacement field. Ambiguity between displacement solutions multiplies when the realistic possibility of combined deformation modes is considered.

To achieve a unique modeled displacement field that correctly describes a real displacement field, the real displacement field must be a simple one. By this we mean that either (1) a single deformation mode is responsible for the majority of surface displacement and contributions from other modes can be assumed to be negligible, or (2) the displacement field can be approximated by no more than two deformation modes, and the observed phase gradient is uniform, such that each contributing mode may be described by a single orientation and magnitude pair. If fringes are curved or the phase gradient is variable, not only the orientation or magnitude of either mode, but also how or whether it varies across the RSVP would need to be constrained. This would be intractable without extensive field measurements.

In the single mode case, we can conduct analytical inversion using equations in Sections 6.2–6.4 directly on the unwrapped phase in each RSVP. In a two-mode case, we first split the unwrapped phase in each RSVP into two components corresponding with the contributions of each mode following Eqn (10).  $\hat{\alpha}_f$ ,  $\hat{\alpha}_{f1}$ ,  $\hat{\alpha}_{f2}$  are unit vectors pointing in the phase gradient direction and the phase gradient directions associated with the two component displacement modes.  $s$ ,  $s_1$ ,  $s_2$  are the magnitudes of the phase gradient and the magnitudes of the phase gradients associated with each component mode:

$$\hat{\alpha}_f s = \begin{bmatrix} \hat{\alpha}_{f1} & \hat{\alpha}_{f2} \end{bmatrix} \begin{bmatrix} s_1 \\ s_2 \end{bmatrix} \quad (10)$$

We then invert displacement fields associated with each component of the phase gradient individually and sum them to obtain the total, two-mode modeled displacement field.

In this work, as outlined in Sections 6.6 and 6.7, we use a combination of environmental context and elimination of modes or mode combinations requiring clearly non-physical model results to constrain model ambiguity. While our reasoning is site specific, the examples described here provide a framework to guide successful application of this method at other sites also.

## 6.2 Analytical inverse method for radially symmetric modes

Since radially symmetric modes can only produce phase gradients parallel or perpendicular to  $\alpha_l$ , we begin by calculating the look-parallel ( $\alpha_{\parallel}$ ) and look-perpendicular ( $\alpha_{\perp}$ ) components of the phase slope across each RSVP according to Eqns (11)–(12), where  $\alpha_{\text{diff}}$  is the interior angle between  $\alpha_l$  and  $\alpha_f$ :

$$\frac{\partial \phi}{\partial \alpha_{\parallel}} = s \cos(\alpha_{\text{diff}}) \quad (11)$$

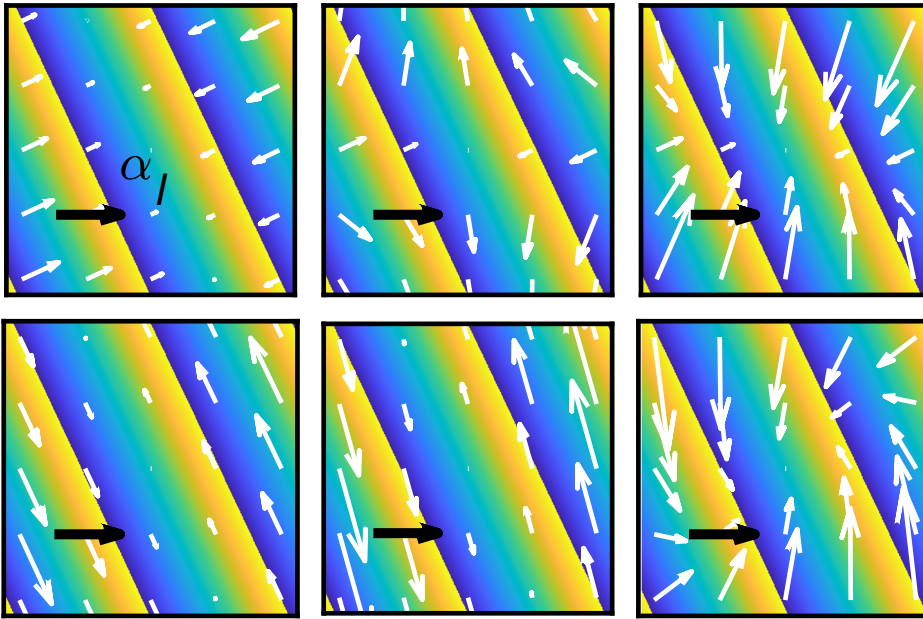


**Figure 4.** Same fringe pattern obtained from the same  $\alpha_l$  (black arrow) can be produced by a myriad of different surface displacement fields (white arrows), that all share the same line-of-sight displacement component.

$$\frac{\partial \phi}{\partial \alpha_{\perp}} = s \sin \alpha_{\text{diff}} \tag{12}$$

We take the average of each slope component,  $\overline{\partial \phi / \partial \alpha_{\parallel}}$ , and  $\overline{\partial \phi / \partial \alpha_{\perp}}$ , across each RSVP to account for isotropic radial convergence and rigid rotation.

Displacement magnitude in these radially symmetric modes scales with distance from a center of deformation. We cannot define this center in an absolute reference frame due to the  $2\pi$  ambiguity in observed  $\phi$ , but the center of relative deformation may be chosen arbitrarily with no impact on modeled strain. We assign the centroid of each RSVP as the center of relative deformation for simplicity.

For each RSVP, we calculate the distance,  $d$ , from the centroid to each pixel. The magnitude of relative radial,  $\Delta d_{\text{rad}}$ , or rotational,  $\Delta d_{\text{rot}}$ , displacement at each pixel is then calculated according to Eqn (13) or (14) where  $\theta$  is the elevation angle from the satellite to a pixel:

$$\Delta d_{\text{rad}} = \frac{\overline{\partial \phi}}{\partial \alpha_{\parallel}} d \frac{-\lambda}{4\pi \cos(\theta)} \tag{13}$$

$$\Delta d_{\text{rot}} = \frac{\overline{\partial \phi}}{\partial \alpha_{\perp}} d \frac{-\lambda}{4\pi \cos \theta} \tag{14}$$

The displacement  $\Delta d_{\text{rad}}$  is positive in the direction pointing from the RSVP centroid to the center of each RSVP pixel,  $\alpha_{\text{rad}}$ . We convert  $\Delta d_{\text{rad}}$  to easting and northing displacements  $u_{\text{rad}}$ ,  $v_{\text{rad}}$  via Eqns (15) and (16), below:

$$u_{\text{rad}} = \Delta d_{\text{rad}} \cos \alpha_{\text{rad}} \tag{15}$$

$$v_{\text{rad}} = \Delta d_{\text{rad}} \sin \alpha_{\text{rad}} \tag{16}$$

$\Delta d_{\text{rot}}$  is perpendicular to  $\alpha_{\text{rad}}$ , either in a clockwise direction, indicated by  $(\hat{\alpha}_f \times \hat{\alpha}_l) < 0$ , or counter-clockwise direction, indicated by  $(\hat{\alpha}_f \times \hat{\alpha}_l) > 0$ , where  $\hat{\alpha}_f$  and  $\hat{\alpha}_l$  are unit vectors pointing in the  $\alpha_f$  and  $\alpha_l$  directions, respectively. Thus, the easting and northing components of rotation  $u_{\text{rot}}$ ,  $v_{\text{rot}}$  are calculated via

Eqns (17) and (18).

$$u_{\text{rot}} = \begin{cases} \Delta d_{\text{rot}} \sin(\alpha_{\text{rot}}) & (\hat{\alpha}_f \times \hat{\alpha}_l) < 0 \\ -\Delta d_{\text{rot}} \sin(\alpha_{\text{rot}}) & (\hat{\alpha}_f \times \hat{\alpha}_l) > 0 \end{cases} \tag{17}$$

$$v_{\text{rot}} = \begin{cases} -\Delta d_{\text{rot}} \cos(\alpha_{\text{rot}}) & (\hat{\alpha}_f \times \hat{\alpha}_l) < 0 \\ \Delta d_{\text{rot}} \cos(\alpha_{\text{rot}}) & (\hat{\alpha}_f \times \hat{\alpha}_l) > 0 \end{cases} \tag{18}$$

### 6.3 Analytical inverse method for axially symmetric modes

For axially symmetric modes, we begin by calculating the horizontal projection,  $\Delta r_{\text{hz}}$ , of recorded line-of-sight displacement using Eqn (19):

$$\Delta r_{\text{hz}} = \frac{-\lambda \phi_{\text{unw}}}{4\pi} \frac{1}{\cos \theta} \tag{19}$$

For these modes, displacement magnitude scales with distance from an axis of deformation rather than a single central point. We again cannot determine the absolute location of deformation axes but choose the line  $\phi_{\text{unw}} = 0$  in each RSVP as the axis of relative deformation for simplicity. We calculate the magnitudes of horizontal displacement for axial divergence,  $\Delta d_{\text{ax}}$ , or simple shear,  $\Delta d_{\text{sh}}$ , that yield  $\Delta r_{\text{hz}}$  when projected onto the look direction as Eqns (20) and (21) below:

$$\Delta d_{\text{ax}} = \frac{\Delta r_{\text{hz}}}{\cos \alpha_{\text{diff}}} \tag{20}$$

$$\Delta d_{\text{sh}} = \frac{\Delta r_{\text{hz}}}{\sin \alpha_{\text{diff}}} \tag{21}$$

Axial divergence gives rise to fringes with  $\alpha_f$  parallel to the direction of displacement, so we calculate the easting and northing components  $u_{\text{ax}}$ ,  $v_{\text{ax}}$  as (22) and (23).

$$u_{\text{ax}} = \Delta d_{\text{ax}} \cos \alpha_f \tag{22}$$

$$v_{\text{ax}} = \Delta d_{\text{ax}} \sin \alpha_f \tag{23}$$

Shear deformation produces fringes with  $\alpha_f$  perpendicular to the direction of motion, with  $(\hat{\alpha}_f \times \hat{\alpha}_1) < 0$  indicating right lateral simple shear, and  $(\hat{\alpha}_f \times \hat{\alpha}_1) > 0$  indicating left lateral simple shear. Easting and northing components,  $u_{sh}$ ,  $v_{sh}$  are calculated as Eqns (24) and (25).

$$u_{sh} = \begin{cases} \Delta d_{sh} \sin(\alpha_f) & (\hat{\alpha}_f \times \hat{\alpha}_1) < 0 \\ -\Delta d_{sh} \sin(\alpha_f) & (\hat{\alpha}_f \times \hat{\alpha}_1) > 0 \end{cases} \quad (24)$$

$$v_{sh} = \begin{cases} -\Delta d_{sh} \cos(\alpha_f) & (\hat{\alpha}_f \times \hat{\alpha}_1) < 0 \\ \Delta d_{sh} \cos(\alpha_f) & (\hat{\alpha}_f \times \hat{\alpha}_1) > 0 \end{cases} \quad (25)$$

#### 6.4 Analytical inverse method for translation

To model rigid translations, we begin by calculating the slope,  $s_\theta$ , and azimuth,  $\alpha_\theta$  of the spatial gradient in elevation angle across the interferogram, as well as the component of phase slope parallel to this gradient  $\partial\phi/\partial\alpha_\theta$ . We differentiate Eqn (4), in an arbitrary, horizontal dimension,  $h$ , continuing our assumption of no vertical displacement to obtain Eqn (26).

$$\frac{\partial\phi}{\partial h} = \frac{4\pi}{\lambda} \left( \frac{\partial d_h}{\partial h} \cos\theta - d_h \sin\theta \frac{\partial\theta}{\partial h} \right) \quad (26)$$

In the absence of strain,  $d_h$  contains only rigid translation,  $d_{tran}$ , and (26) simplifies to (27)

$$\frac{\partial\phi}{\partial h} = \frac{4\pi}{\lambda} \left( -d_{tran} \frac{\partial\theta}{\partial h} \sin\theta \right) \quad (27)$$

If we choose  $h$  to be the direction of the gradient in elevation angle, Eqn (27) may be rearranged to solve for translation, giving (28):

$$d_{tran} = \frac{-\lambda(\partial\phi/\partial\alpha_\theta)}{4\pi(s_\theta \sin\theta)} \quad (28)$$

If the assumption that the phase gradient contains no strain is incorrect (i.e. displacement is not uniform across an RSVP), this method will overestimate translation magnitudes due to the additional component of  $\partial\phi/\partial\alpha_\theta$  contributed by any gradient in surface displacement. To minimize this overestimation, we take the median value of  $d_{tran}$  to be the best estimate of translation across each RSVP. This median displacement is then divided into easting and northing components  $u_{tran}$  and  $v_{tran}$  according to Eqns (29) and (30):

$$u_{tran} = -d_{tran} \cos\alpha_\theta \quad (29)$$

$$v_{tran} = d_{tran} \sin\alpha_\theta \quad (30)$$

#### 6.5 Strain calculation from modeled horizontal displacements

From each modeled displacement field, we can derive first and second principal components of strain,  $\varepsilon_1$  and  $\varepsilon_2$ . Normal strains on planes parallel to the  $x$  (easting) and  $y$  (northing) directions  $\varepsilon_{xx}$  and  $\varepsilon_{yy}$  and shear strain on these planes  $\tau_{xy}$  are calculated according to Eqns (31)–(33).  $\tau_{xy}$  may include both pure and simple shear components,

depending upon the orientation of the strain field:

$$\varepsilon_{xx} = \frac{\Delta u}{\Delta x} \quad (31)$$

$$\varepsilon_{yy} = \frac{\Delta v}{\Delta y} \quad (32)$$

$$\tau_{xy} = \frac{1}{2} \left( \frac{\Delta u}{\Delta y} + \frac{\Delta v}{\Delta x} \right) \quad (33)$$

We can then calculate the angle of first principal strain according to Eqn (34),

$$\theta_p = \text{atan} \left( \frac{2\tau_{xy}}{\varepsilon_{xx} - \varepsilon_{yy}} \right) \frac{1}{2} \quad (34)$$

and calculate  $\varepsilon_1$  and  $\varepsilon_2$  as Eqn (35):

$$\begin{bmatrix} \varepsilon_1 & 0 \\ 0 & \varepsilon_2 \end{bmatrix} = \begin{bmatrix} \cos(\theta_p) & \sin(\theta_p) \\ -\sin(\theta_p) & \cos(\theta_p) \end{bmatrix} \begin{bmatrix} \varepsilon_{xx} & \tau_{xy} \\ \tau_{xy} & \varepsilon_{yy} \end{bmatrix} \times \begin{bmatrix} \cos(\theta_p) & -\sin(\theta_p) \\ \sin(\theta_p) & \cos(\theta_p) \end{bmatrix} \quad (35)$$

We use the convention that compressive strains are positive, and  $|\varepsilon_1| > |\varepsilon_2|$ .

#### 6.6 Addressing model ambiguity in Elson Lagoon

Of the 15 Sentinel 1 interferograms which maintain adequate coherence across Elson Lagoon for analysis (Fig. 5), ten contain RSVPs in which the phase gradient is monotonic in the look direction, meeting our criteria for assuming predominantly horizontal motion as discussed in Section 4. Of these ten interferograms (Figs 5a–e, g–i, l, m), there are nine in which mean  $\alpha_f$  across Elson Lagoon remains near-parallel to  $\alpha_1$  ( $|\alpha_{diff}| < 6^\circ$ ). These nine interferograms, outlined in red in Figure 5, include interferograms from both ascending and descending orbits, some of which overlap in time by several days.

We use the following reasoning to infer radial convergence is the single dominant deformation mode during these nine images.

- (1) Rotational displacement cannot produce fringes in the observed orientation.
- (2) Simple shear solutions would require implausibly large strains  $> 10^{-1}$  at locations where  $\alpha_f$  switches from clockwise to counter-clockwise of  $\alpha_1$  (e.g. Fig. 6 a), implying switches between left and right lateral shear (Fig. 6b). Strains of this magnitude would certainly lead to the formation of cracks or ridges recognizable in the underlying SAR imagery and diminished interferometric coherence, neither of which are observed.
- (3) To maintain the near-parallel relationship between average  $\alpha_f$  and  $\alpha_1$  axial convergence and simple shear would have needed to change orientation in synchrony with look direction. Similarly, translation direction would have needed to reverse in tandem with changes in look direction. There is no physical reason for this to happen consistently, particularly given temporal overlap between some interferograms acquired with differing look directions.

This leaves radial displacement as the only plausible main deformation mode making a majority contribution to the nine



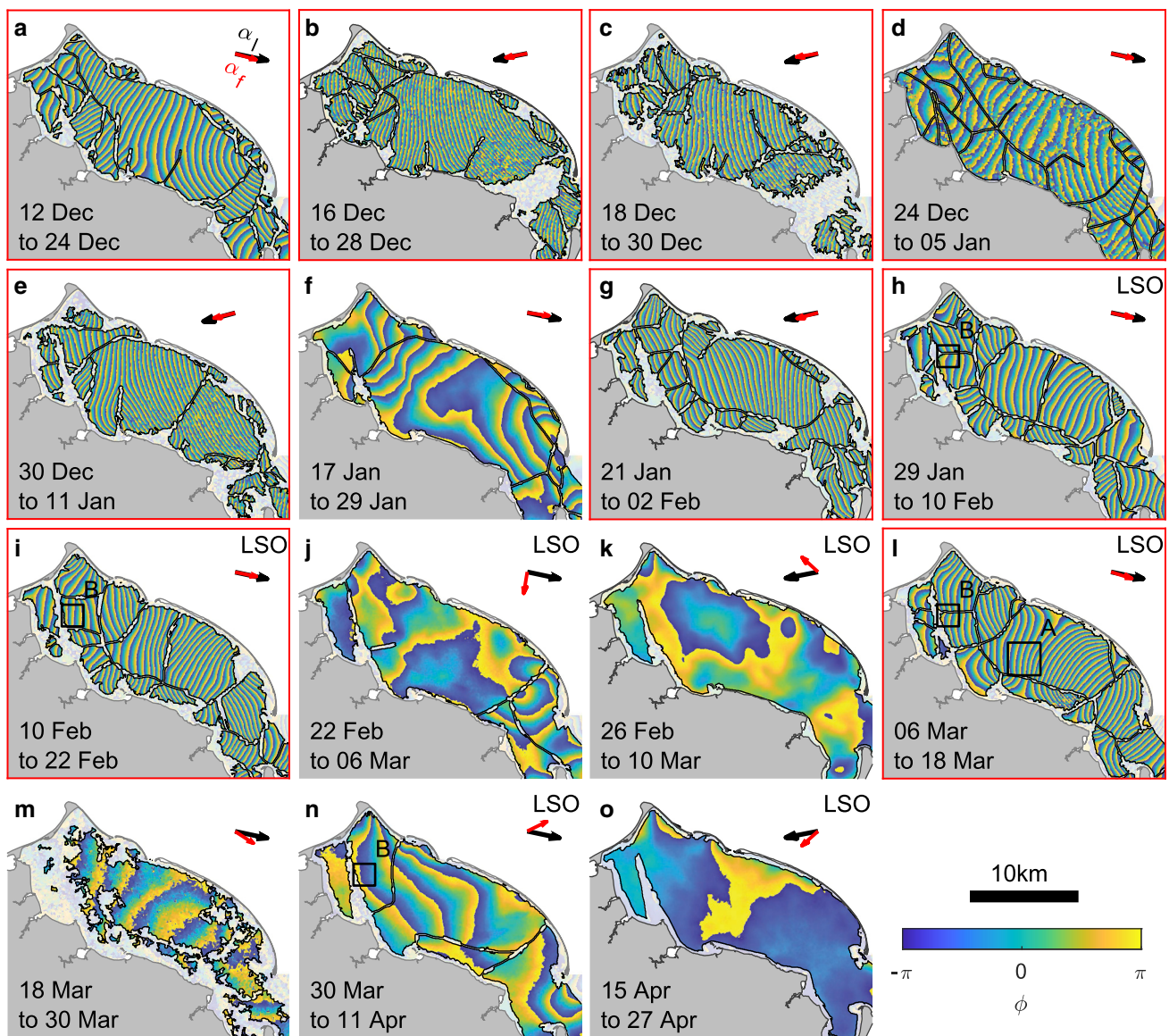


**Figure 5.** All 15 analyzed S1 interferograms over Elson Lagoon. Black arrows mark the mean look direction,  $\alpha_l$ , from each pixel in the lagoon to the satellite. Red arrows mark the average azimuth direction of the phase gradient,  $\alpha_f$ , within the lagoon. Red outlines highlight the nine interferograms (a–e, g–i, l) in which  $\alpha_f$  remains near-parallel to  $\alpha_l$ . Interferograms annotated ‘LSO’ in the top-right corner are interferograms for which point strain measurements from the LSO corresponding with both the start and end points of the interferogram exist. Box labeled ‘A’ marks the location of detail plots shown in Figure 6. Boxes labeled ‘B’ mark the location of the detail plots shown in Figure 9.

interferograms outlined in red in Figure 5. Radial displacement produces fringes with  $\alpha_f$  parallel to  $\alpha_l$ , and is plausible over 12 d periods in the context of the sheltered, landlocked lagoon.

### 6.7 Addressing model ambiguity in the Chukchi Sea

The relationship between  $\alpha_f$  and  $\alpha_l$  in TDX interferograms over drifting pack ice in the Chukchi Sea is more heterogeneous than that in Elson Lagoon (Figs 10a, e, i). In total, 84% of pixels reside in RSVPs in which the phase gradient points counter-clockwise of the look direction, but there are several cases of adjacent regions exhibiting nearly opposite phase gradient directions (e.g. white ellipse in Fig. 10e). In total, 48% of pixels reside in RSVPs where  $\alpha_f$  is near-perpendicular ( $\pm 10^\circ$ ) to  $\alpha_l$ , and  $\alpha_f$  is near-parallel ( $\pm 10^\circ$ ) to  $\alpha_l$  within only one RSVP (containing 14% total pixel area).

We infer radial convergence is an unlikely contributor to these phase gradients as it can only produce phase gradients with  $\alpha_f$  parallel to  $\alpha_l$ . Additionally, we expect radial convergence to result

from thermal rather than dynamic forcing. A 10 s interferogram interval is much shorter than expected timescales of both diurnal and synoptic temperature changes that could lead to such strains. This leaves rotation, translation, simple shear and axial convergence as plausible deformation modes.

The uniformity of phase gradients across Chukchi Sea RSVPs suggests rigid motions are the most likely contributors. We expect non-rigid deformations to exhibit spatial variability, with largest magnitudes nearest to locations of contact with other RSVPs. Before ruling out non-rigid motion entirely, however, we pursue two, two-mode inversions: one combining translation and rotation, and one combining simple shear and axial convergence.

Translation and rotation produce nearly orthogonal fringes, allowing us to confidently separate their contributions to the phase gradient. We model the entire look parallel component of the phase gradient as the result of translation, and the entire look-perpendicular component of the phase gradient as the result of rotation.

Simple shear and axial convergence can produce fringes in any orientation. We lack independent measurements to quantitatively

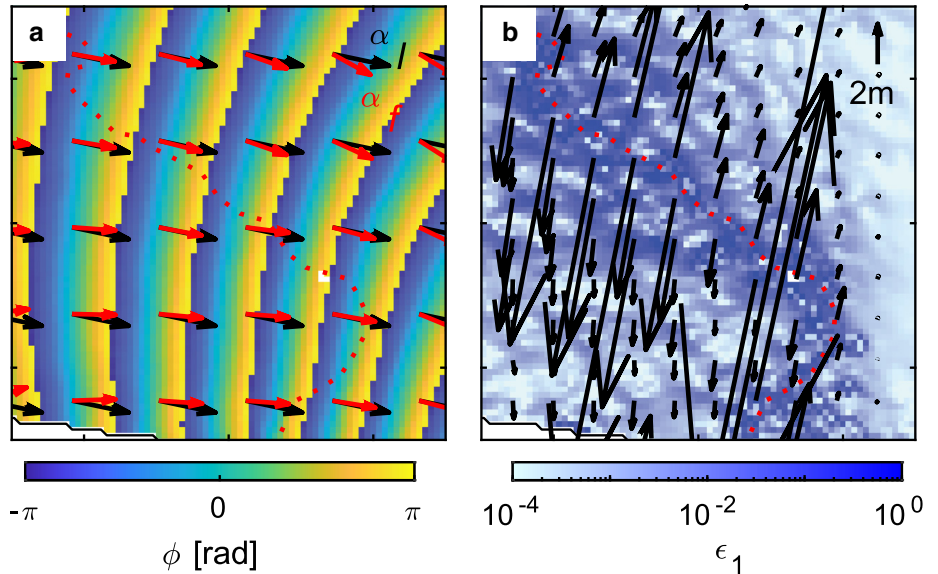


**Figure 6.** Details from the Sentinel 1 interferogram spanning 6–18 March 2019 (Fig. 5f, box ‘A’). (a) In the top-right portion of the panel, above the red dashed line,  $\alpha_f$  (red arrows) points counter-clockwise of  $\alpha_l$  (black arrows) indicating right lateral shear, but in the lower left portion,  $\alpha_f$  points clockwise of  $\alpha_l$ , indicating left lateral shear. (b) Inverse modeled relative displacements (black arrows) in this area show unrealistically large divergent displacements of several meters and correspond to unrealistically large strains  $>0.1$  (color bar) in the zone of transition from right to left lateral shear.

inform prescription of orientation or magnitude of either mode. Instead, we explore inverse solutions corresponding with all possible combinations of 50 shear orientations and 50 axial convergence orientations evenly spaced between  $-90^\circ$  and  $90^\circ$ . The axial symmetry of these modes makes inclusion of orientations beyond this range redundant.

Maximum principal strains calculated from non-rigid model results approach infinity where  $\alpha_f$  due to shear approaches  $\alpha_l$  or  $\alpha_f$  due to convergence approaches  $\alpha_l \pm \pi/2$ . However, minimum primary principal strains are finite, giving a meaningful floor to possible non-rigid strain magnitude in each RSVP. Across the three TDX interferograms analyzed, the 5th and 95th percentiles of minimum principal strain are  $-4.19 \times 10^{-5}$  and  $7.64 \times 10^{-5}$ . Over 10 s intervals we expect observed non-rigid strain to be primarily elastic, requiring a proportional change in stress. Assuming cold ice with an elastic modulus on the order of  $10^9$  Pa, this proportional stress would be on the order of  $10^4$  Pa (Timco and Weeks, 2010). This is the same order of magnitude as the largest observed stresses in situ sea ice (e.g. Richter-Menge and others, 2002; Parno and others, 2022). The ice cannot support such stress

changes over 10 s intervals over such large areas and remain intact, so the TDX interferograms cannot be the result of non-rigid deformation.

**7. Results**

**7.1 Single-mode modeled displacement and strain in landlocked ice from InSAR**

In Elson Lagoon, modeled isotropic radial convergence displacements reproduce most of the observed interferometric phase gradient. Correlation coefficient values between  $\phi_{umw}$  and synthetic phase,  $\phi_{synth}$ , calculated from modeled displacements exceed 0.89 for the ten interferograms recording predominantly horizontal displacement. Residual phase remaining after subtracting  $\phi_{synth}$  from  $\phi_{umw}$  indicates anisotropy in the real displacement field not captured by the inversion, but the correlation coefficients near 1 give us confidence displacement results are accurate to a first-order approximation. Modeled  $\epsilon_1$  are nearly exclusively convergent (positive). Median modeled  $\epsilon_1$  within each RSVP in the lagoon reach maximum values on the order of  $10^{-4}$  in December and January and show a decreasing trend over the remainder of the observed season (Fig. 7).

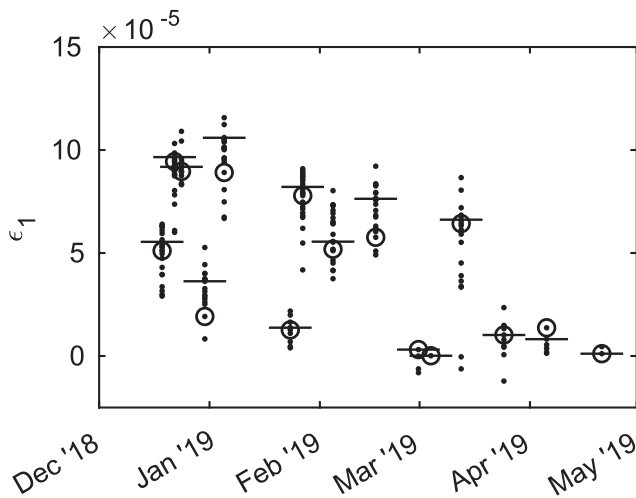


**Figure 7.** Median  $\epsilon_1$  calculated from modeled radial convergence displacements. Dots indicate median values for each RSVP within the lagoon, open circles indicate median  $\epsilon_1$  within the RSVP containing the LSO’s central total station, and horizontal bars indicate median strain across Elson Lagoon as a whole. The width of each horizontal bar spans the 12 d duration of each interferogram.

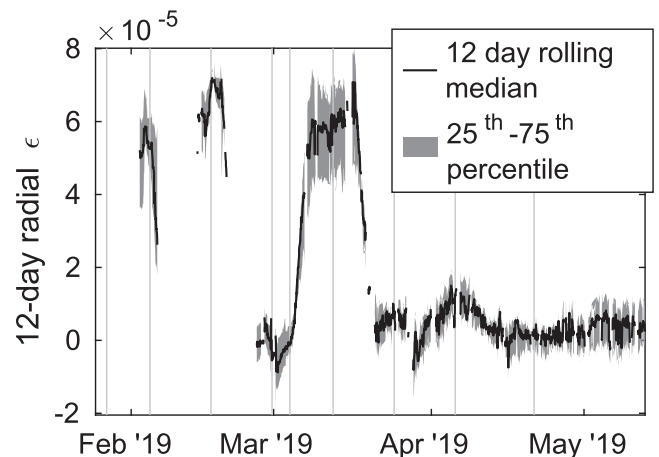


**Figure 8.** Rolling 12 d radial strain recorded between each LSO reflector and the central total station throughout spring 2019. Vertical gray lines indicate the central day of each interferogram during the plotted time period.

## 7.2 Displacement and strain in landlocked ice from point observations

Median LSO-observed radial strains over a 12 d rolling window show convergent strains throughout the winter, with temporal variability between periods of activity and quiescence (Fig. 8). Largest strains on the order of  $10^{-5}$  occur in February and March, followed by smaller strains in April and May. The few short periods of divergence evident in Figure 8 are near the accuracy limit of the method.

## 7.3 Comparison between observed and modeled displacements on Elson Lagoon

We have corresponding LSO observations near both start and end times of seven interferograms over Elson Lagoon (annotated in Fig. 5). We interpolate LSO range and azimuth measurements to these start and end times and calculate displacement during each interferogram from these interpolated values. We exclude values interpolated over gaps in the reflector time series longer than 20 min, as well as values from reflectors not located in the same RSVP as the central total station. We then interpolate modeled displacements from pixel centers to the positions of each retroreflector. To shift these into the same reference frame as LSO observations, we subtract modeled displacement at the central total station from these modeled reflector displacements.

Only four of these seven interferograms, those starting on 29 January, 10 February, 6 March and 30 March, show a monotonic phase gradient in the RSVP containing the LSO's central total station, indicating vertical deformation may be neglected. Correlation coefficients between modeled and observed easting displacements during all four of these interferograms and between modeled and observed northing displacements during all but the interferogram beginning on 30 March are better than 0.9, with little deformation observed by either method in that interferogram (Fig. 9).

## 7.4 Two-mode modeled strain and displacement in drifting pack ice

Over drifting pack ice in the Chukchi Sea, modeled rotation (Figs 10b, f, j) accounts for the majority of the phase gradient in most RSVPs. In total, 95% of RSVPs require edge-to-edge rotational displacements, calculated as twice the maximum  $\Delta d_{\text{rot}}$  in each RSVP, of 20 cm or less. Half of all RSVPs require only 4.5 cm or less edge-to-edge rotation. Most of the remaining phase gradient is accounted for by modeled translation (Figs 10c, g, k). In total, 95% of RSVPs require translations of 5.3 m or less, corresponding to speeds  $\leq 0.53 \text{ m s}^{-1}$  over 10 s interferogram intervals. Half of RSVPs require modeled translations corresponding with velocities  $\leq 0.16 \text{ m s}^{-1}$ .

## 8. Discussion

### 8.1 Implications of strain results

Over Elson Lagoon, single-mode radial convergence displacements indicate largest median strains on the order of  $10^{-4}$ , or 12 d average strain rates on the order of  $10^{-10} \text{ s}^{-1}$ . These strains are likely caused by thermal forcing, both because of the sheltered nature of the lagoon, and because thermal strain does not require proportional thermal stress. If the strains were instead dynamically forced, elastic strains they would correspond to stresses on the order of  $10^5 \text{ Pa}$ , assuming cold sea ice with a Young's modulus on the order of  $10^9 \text{ Pa}$  (Timco and Weeks, 2010). This would be larger than the expected strength of sea ice at these scales.

In TDX interferograms over drifting sea ice, we find the observed fringe patterns can be replicated with rotations requiring displacements of tens of centimeters or less, and translations at speeds of  $\text{m s}^{-1}$  or less. Although the ice cover is consolidated during these interferograms, very little space is needed to accommodate tens of centimeters of differential motion between RSVPs, and small, jostling rotations make sense in the context of likely

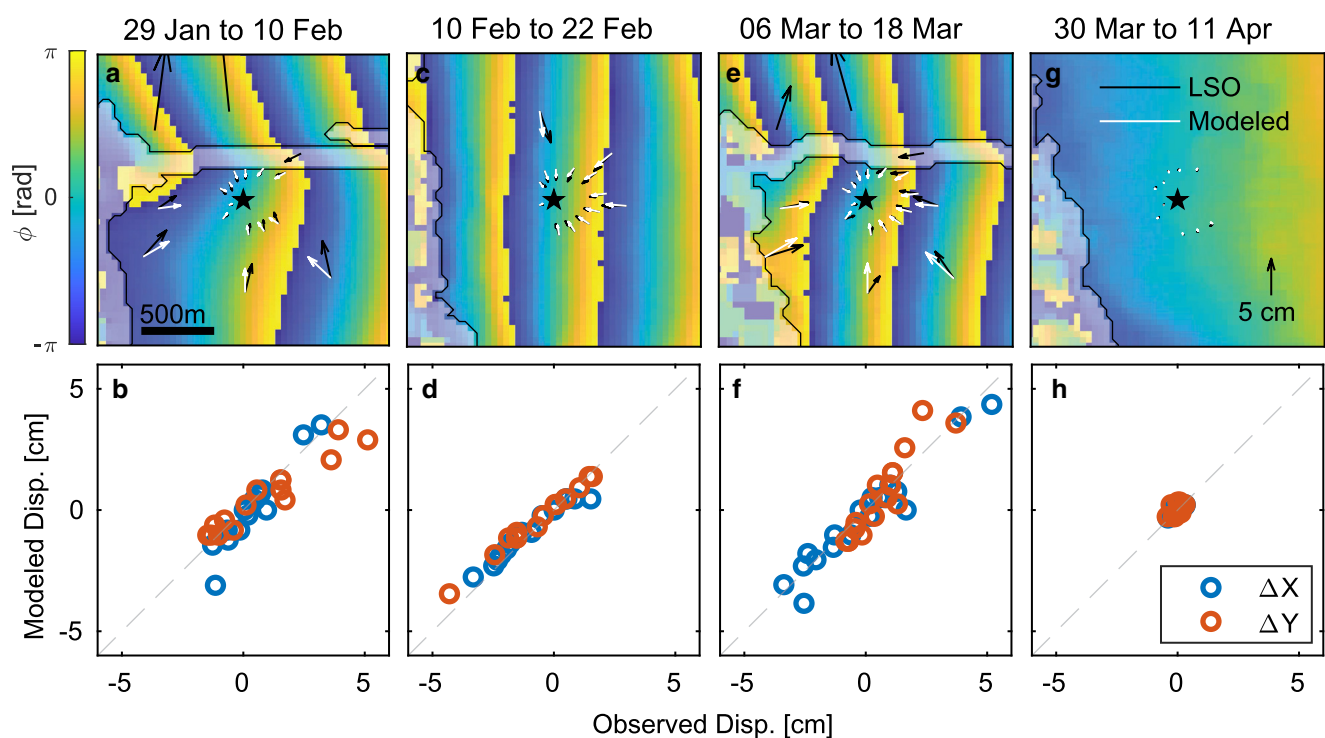


**Figure 9.** Interferometric phase gradients are monotonic along the look direction in four interferograms for which we have LSO data for comparison. Black and white arrows show LSO-observed displacements and modeled displacements. Comparison between modeled and observed easting and northing displacements (bottom row) shows good agreement.

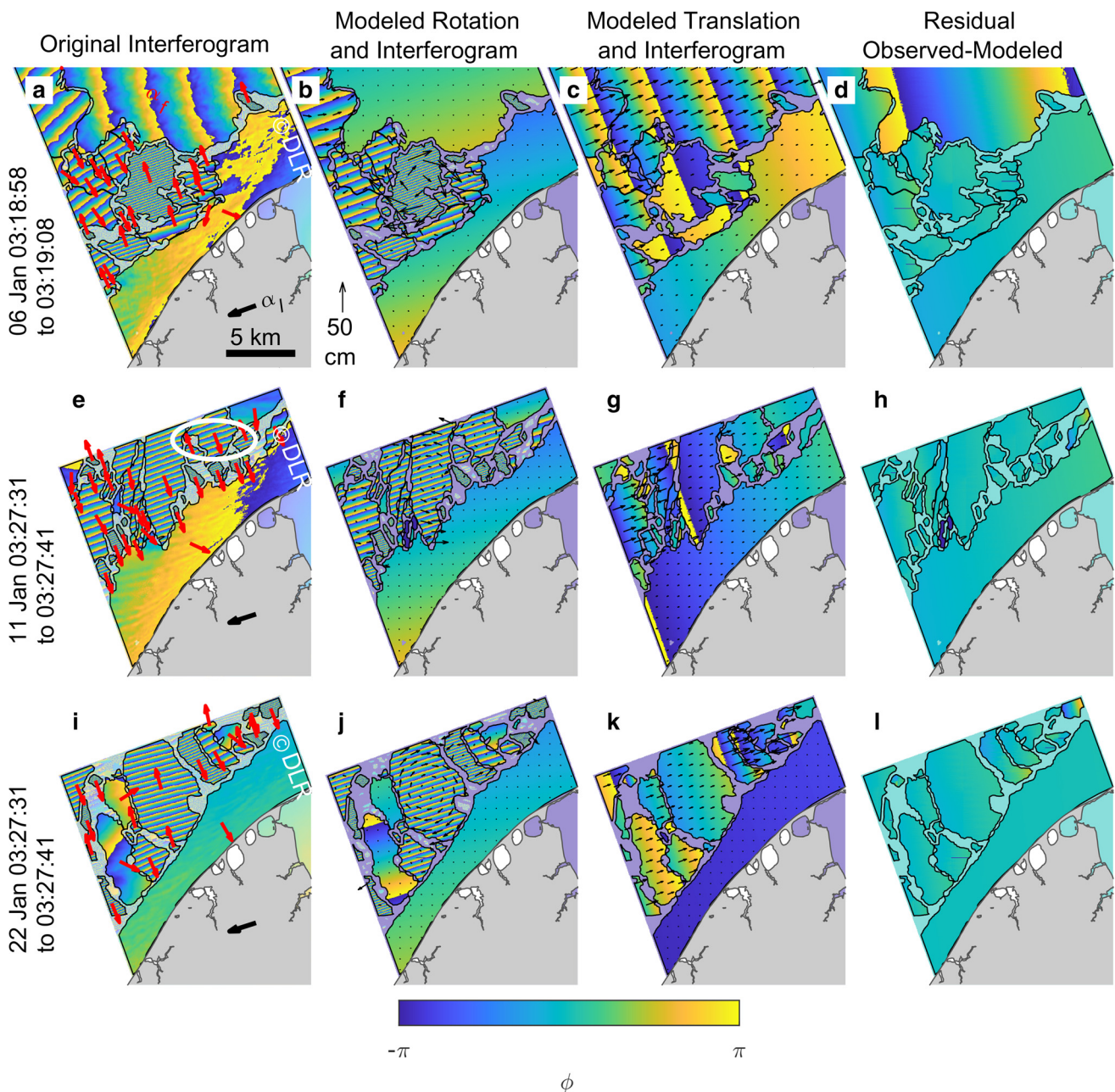


**Figure 10.** RSVPs in TDX interferograms (a, e, i) exhibit straight, parallel fringes with differing phase slopes and orientations (red arrows). Modeled rotation (black arrows, b, f, j), explains much of the observed phase gradient. Translation accounts for much of the residual left behind by rotation (c, g, k). Residual phase not accounted for by combined modeled rotation and modeled translation is shown in (d, h, l).

off-center collisions between RSVPs. Modeled translations are minimum estimates, since InSAR is only sensitive to the component of translation parallel to the gradient in elevation angle across the image, but modeled velocities fall within the expected range for drifting sea ice in the study area (Mahoney and others, 2015). Rotations in the study area have not been previously quantified, but modeled rotations fall within the range calculated from interferograms off the coast of Greenland (Scheiber and others, 2011).

### 8.2 Physical interpretation of RSVPs

RSVPs represent mechanically contiguous ice experiencing continuous strain bounded by active fractures accommodating brittle displacement. Their presence in both sheltered, landlocked sea ice and drifting pack ice show RSVPs are ubiquitous across differing dynamic regimes. While they resemble ice ‘flocs’ which can be

otherwise difficult to define in areas of consolidated ice, they are transient features. Within Elson Lagoon, where we observe the same ice surface throughout the winter, some RSVP boundaries persist across many interferograms, while others appear and disappear between one interferogram and the next, even between interferograms which overlap. This indicates either thermodynamic healing, or simply deactivation, of fractures in response to changing forcing. This transience highlights the importance of spatially dense displacement measurements that allow delineation of mechanically continuous ice to studies pursuing in situ measurements of continuous strain.

### 9. Conclusions

Interferograms offer the ability to identify discrete regions of continuous sea-ice deformation and the boundaries between them with greater precision than is possible using sparse point

measurements. In doing so, our results highlight the discrete nature of sea-ice deformation at the ‘floe scale’ from tens of meters to kilometers, which is missed by large-scale continuum sea-ice models. The analytical inverse model we describe here provides a method for quantifying 2-D strain within such continuous regions with improved computational efficiency and finer strain resolution than previous, iterative inverse methods described by Dammann and others (2016, 2018). We additionally include translation in this inverse framework, which was not treated by these previous inverse methods.

Without the ability to use data from multiple look directions, the inverse model is subject to ambiguities between horizontal and vertical motions and between different deformation modes that result in equivalent interferometric fringe patterns. However, by limiting application of the model to regions without significant fringe curvature (i.e. simple, monotonic phase gradients), we show that it is possible to accurately estimate 2-D horizontal displacement from a single interferogram. For example, after excluding interferograms over Elson Lagoon that exhibited undulating phase gradients indicative of combined horizontal and vertical deformation, we are able to derive a first-order approximation of 2-D displacement and strain in the lagoon (Section 7.1). We validated these results by comparison with in situ observations (Section 7.3), but we expect the inverse model would be similarly successful in observing thermal deformation in other areas of sheltered, landlocked ice using the same selection criteria we use here, even without additional field measurements.

In drifting ice where more complex forcing scenarios are possible, we show that utilizing a short-interval interferogram can help to constrain model results. At our Chukchi Sea study site, we found TDX interferograms acquired over 10 s intervals contained fringes with near-zero curvature. Moreover, we were able to exclude large strains that would have been required to produce the observed fringe patterns through non-rigid deformation (Section 6.7) and conclude these interferograms must record primarily rigid rotation and translation instead (Section 7.4). While such short interferogram intervals are not available from currently operating satellite constellations, this provides a new tool for constraining sea-ice motion from past data. In scenarios with even more complex forcing possibilities, such as unsheltered landfast ice over 12 d intervals, additional information from concurrent field measurements of displacement or more complex modeling that better accounts for sea-ice rheology would be required to achieve accurate model results.

**Supplementary material.** The supplementary material for this article can be found at <https://doi.org/10.1017/aog.2024.29>.

**Acknowledgements.** This work was supported by funding from the Office of Naval Research award No. N0001419MP00167. TanDEM-X data were provided free of charge by the German Aerospace Center (DLR) through science proposal (XTI\_GLAC6921). Sentinel-1 data are provided free of charge by the European Union Copernicus program and were accessed through the Alaska Satellite Facility (ASF).

**Author contributions.** All authors contributed significantly to interpretation of results as well as the structure and content of the paper. E.R.F. performed the majority of the analytical inverse model development, conducted all interferometric processing and inverse model calculations, and led the writing of the paper; A.R.M. conducted initial analytical inverse model development, co-wrote the proposal that funded this work and reviewed the manuscript; D.O.D. wrote the science proposal through which TDX data were accessed, contributed to inverse model development and reviewed the manuscript; C.P. contributed to LSO data collection, provided code for LSO data processing, co-wrote the proposal that funded this work and reviewed the manuscript; J.H. co-wrote the proposal that funded this work and reviewed the manuscript.

## References

- Berg A, Dammert P and Eriksson LEB** (2015) X-band interferometric SAR observations of Baltic fast ice. *IEEE Transactions on Geoscience and Remote Sensing* **53**(3), 1248–1256. doi: [10.1109/TGRS.2014.2336752](https://doi.org/10.1109/TGRS.2014.2336752)
- Chen Z and 6 others** (2021) InSAR monitoring of Arctic landfast sea ice deformation using L-band ALOS-2, C-band Radarsat-2 and Sentinel-1. *Remote Sensing* **13**(22), 1–22. doi: [10.3390/rs13224570](https://doi.org/10.3390/rs13224570)
- Dammann DO, Eicken H, Meyer FJ and Mahoney AR** (2016) Assessing small-scale deformation and stability of landfast sea ice on seasonal timescales through L-band SAR interferometry and inverse modeling. *Remote Sensing of Environment* **187**, 492–504. doi: [10.1016/j.rse.2016.10.032](https://doi.org/10.1016/j.rse.2016.10.032)
- Dammann DO and 5 others** (2018) Evaluating landfast sea ice stress and fracture in support of operations on sea ice using SAR interferometry. *Cold Regions Science and Technology* **149**(January), 51–64. doi: [10.1016/j.coldregions.2018.02.001](https://doi.org/10.1016/j.coldregions.2018.02.001)
- Dammann DO, Eriksson LEB, Mahoney AR, Eicken H and Meyer FJ** (2019) Mapping pan-Arctic landfast sea ice stability using Sentinel-1 interferometry. *The Cryosphere* **13**, 557–577. doi: [10.5194/tc-13-557-2019](https://doi.org/10.5194/tc-13-557-2019)
- Dammert PBG, Lepparanta M and Askne J** (1998) SAR interferometry over Baltic Sea ice. *International Journal of Remote Sensing* **19**(16), 3019–3037. doi: [10.1080/014311698214163](https://doi.org/10.1080/014311698214163)
- Damsgaard A, Adcroft A and Sergienko O** (2018) Application of discrete element methods to approximate sea ice dynamics. *Journal of Advances in Modeling Earth Systems* **10**(9), 2228–2244. doi: [10.1029/2018MS001299](https://doi.org/10.1029/2018MS001299)
- Dansereau V, Weiss J, Saramito P and Lattes P** (2016) A Maxwell elastobrittle rheology for sea ice modelling. *The Cryosphere* **10**(3), 1339–1359. doi: [10.5194/tc-10-1339-2016](https://doi.org/10.5194/tc-10-1339-2016)
- Dulam RVS, Fedders ER, Mahoney AR and Kambhamettu C** (2023) ConvSegFormer – A Convolution Aided SegFormer Architecture for Detection of Discontinuities in Wrapped Interferometric Phase Imagery of Sea Ice. Lecture Notes in Computer Science (including subseries Lecture Notes in Artificial Intelligence and Lecture Notes in Bioinformatics) 13886 LNCS, 203–213. doi: [10.1007/978-3-031-31438-4\\_14](https://doi.org/10.1007/978-3-031-31438-4_14)
- Duncan K and Farrell SL** (2022) Determining variability in Arctic sea ice pressure ridge topography with ICESat-2. *Geophysical Research Letters* **49**(18), 1–10. doi: [10.1029/2022GL100272](https://doi.org/10.1029/2022GL100272)
- Evans R, Untersteiner N, Evans RJ and Untersteiner N** (1971) Thermal cracks in floating ice sheets. *Journal of Geophysical Research* **76**(3), 694–703. doi: [10.1029/jc076i003p00694](https://doi.org/10.1029/jc076i003p00694)
- Goldstein RM and Werner CL** (1998) Radar interferogram filtering for geophysical applications. *Geophysical Research Letters* **25**(21), 4035–4038. doi: [10.1029/1998GL900033](https://doi.org/10.1029/1998GL900033)
- Hata Y and Tremblay LB** (2015a) A 1.5-D anisotropic sigma-coordinate thermal stress model of landlocked sea ice in the Canadian Arctic Archipelago. *Journal of Geophysical Research: Oceans* **120**, 8251–8269. doi: [10.1002/2015JC010820](https://doi.org/10.1002/2015JC010820). Received
- Hata Y and Tremblay LB** (2015b) Anisotropic internal thermal stress in sea ice from the Canadian Arctic Archipelago. *Journal of Geophysical Research: Oceans* **120**, 5457–5542. doi: [10.1038/175238c0](https://doi.org/10.1038/175238c0)
- Hibler WD** (1979) A dynamic thermodynamic sea ice model. *Journal of Physical Oceanography* **9**, 815–846.
- Hogenson K and 5 others** (2016) Hybrid Pluggable Processing Pipeline (HyP3): a cloud-based infrastructure for generic processing of SAR data. AGU Fall Meeting Abstracts (IN21B-1740). Available at <https://ui.adsabs.harvard.edu/abs/2016AGUFMIN21B1740H/abstract>
- Hutchings JK, Heil P and Hibler WD** (2005) Modeling linear kinematic features in pack ice. *Monthly Weather Review* **133**, 3481–3497. doi: [10.1029/2008JC005217](https://doi.org/10.1029/2008JC005217)
- Jolivet R and others** (2014) Improving InSAR geodesy using global atmospheric models. *Journal of Geophysical Research: Solid Earth* **119**(3), 2324–2341. doi: [10.1002/2013JB010588](https://doi.org/10.1002/2013JB010588)
- Jolivet R, Grandin R, Lasserre C, Doin MP and Peltzer G** (2011) Systematic InSAR tropospheric phase delay corrections from global meteorological reanalysis data. *Geophysical Research Letters* **38**(17), 1–6. doi: [10.1029/2011GL048757](https://doi.org/10.1029/2011GL048757)
- Kwok R** (2001) Deformation of the Arctic ocean sea ice cover between November 1996 and April 1997: a qualitative survey. In Dempsey JP and Shen HH (eds). *IUTAM Symposium on Scaling Laws in Ice Mechanics and Ice Dynamics. Solid Mechanics and Its Applications*. Dordrecht, Netherlands: Springer, pp. 315–322. doi: [10.1007/978-94-015-9735-7\\_26](https://doi.org/10.1007/978-94-015-9735-7_26)

- Kwok R and Morison J** (2016) Sea surface height and dynamic topography of the ice-covered oceans from CryoSat-2: 2011–2014. *Journal of Geophysical Research: Oceans* **121**, 674–692.
- Li S, Shapiro L, McNutt L and Jeffers A** (1996) Application of satellite of sea radar interferometry to the detection. *Journal of the Remote Sensing Society of Japan* **16**(2), 67–77.
- Libert L, Wuite J and Nagler T** (2022) Automatic delineation of cracks with Sentinel-1 interferometry for monitoring ice shelf damage and calving. *The Cryosphere* **16**(4), 1523–1542. doi: [10.5194/tc-16-1523-2022](https://doi.org/10.5194/tc-16-1523-2022)
- Mahoney AR** (2018) Land fast sea ice in a changing arctic. In Osborne EJ, Richter-Menge J and Jeffries M (eds), *Arctic Report Card 2018*, 99–109. <https://www.arctic.noaa.gov/Report-Card>
- Mahoney A, Eicken H and Shapiro L** (2007) How fast is landfast sea ice? A study of the attachment and detachment of nearshore ice at Barrow, Alaska. *Cold Regions Science and Technology* **47**(3), 233–255. doi: [10.1016/j.coldregions.2006.09.005](https://doi.org/10.1016/j.coldregions.2006.09.005)
- Mahoney AR and 8 others** (2015) Taking a look at both sides of the ice: comparison of ice thickness and drift speed as observed from moored, airborne and shore-based instruments near Barrow, Alaska. *Annals of Glaciology* **56**(69), 363–372. doi:[10.3189/2015AoG69A565](https://doi.org/10.3189/2015AoG69A565)
- Mahoney AR, Dammann DO, Johnson MA, Eicken H and Meyer FJ** (2016) Measurement and imaging of infragravity waves in sea ice using InSAR. *Geophysical Research Letters* **43**(12), 6383–6392. doi: [10.1002/2016GL069583](https://doi.org/10.1002/2016GL069583)
- McKenna R, Loewen A and Crocker G** (2021) A finite element model for the deformation of floating ice covers. *Cold Regions Science and Technology* **182**(December 2020), 103213. doi: [10.1016/j.coldregions.2020.103213](https://doi.org/10.1016/j.coldregions.2020.103213)
- Meyer FJ and 5 others** (2011) Mapping Arctic landfast ice extent using L-band synthetic aperture radar interferometry. *Remote Sensing of Environment* **115**, 3029–3043. doi: [10.1016/j.rse.2011.06.006](https://doi.org/10.1016/j.rse.2011.06.006)
- Moreira A and 5 others** (2013) A Tutorial on Synthetic Aperture Radar. *Geoscience and Remote Sensing Magazine, IEEE* (March).
- Morris K, Li S and Jeffries M** (1999) Meso- and microscale sea-ice motion in the East Siberian Sea as determined from ERS-1 SAR data. *Journal of Glaciology* **45**(150), 370–383. doi: [10.1017/S0022143000001878](https://doi.org/10.1017/S0022143000001878)
- Parno J and 5 others** (2022) Observations of stress-strain in drifting sea ice at floe scale. *Journal of Geophysical Research: Oceans* **127**, 22. doi: [10.1029/2021JC017761](https://doi.org/10.1029/2021JC017761)
- Richter-Menge JA, McNutt SL, Overland JE and Kwok R** (2002) Relating Arctic pack ice stress and deformation under winter conditions. *Journal of Geophysical Research* **107**(10), 15–17. doi: [10.1029/2000jc000477](https://doi.org/10.1029/2000jc000477)
- Rosen PA and 6 others** (2000) Synthetic aperture radar interferometry. *Proceedings of the IEEE* **88**(3), 333–382. doi:[10.1007/978-3-642-11741-1\\_11](https://doi.org/10.1007/978-3-642-11741-1_11)
- Scheiber R and 5 others** (2011) Interferometric sea ice mapping with TanDEM-X: first experiments. *2011 IEEE International Geoscience and Remote Sensing Symposium (IGARSS)*, 3594–3597. doi: [10.1109/IGARSS.2011.6050001](https://doi.org/10.1109/IGARSS.2011.6050001)
- Timco GW and Weeks WF** (2010) A review of the engineering properties of sea ice. *Cold Regions Science and Technology* **60**(2), 107–129. doi: [10.1016/j.coldregions.2009.10.003](https://doi.org/10.1016/j.coldregions.2009.10.003)
- Wang Z and others** (2020) Resolving and analyzing landfast ice deformation by InSAR technology combined with Sentinel-1a ascending and descending orbits data. *Sensors (Switzerland)* **20**(22), 1–16. doi:[10.3390/s20226561](https://doi.org/10.3390/s20226561)
- Werner CL, Wegmüller U and Strozzi T** (2002) *Processing Strategies for Phase Unwrapping for InSAR Applications. 4th European Conference on Synthetic Aperture Radar (EUSAR 2002)*. 353–356.
- West B, O'Connor D, Parno M, Krackow M and Polashenski C** (2022) Bonded discrete element simulations of sea ice with non-local failure: applications to nares strait. *Journal of Advances in Modeling Earth Systems* **14**(6), 1–24. doi: [10.1029/2021MS002614](https://doi.org/10.1029/2021MS002614)
- Woodhouse IH** (2006) *Introduction to Microwave Remote Sensing*. Boca Raton, FL: Taylor and Francis.